RSC Advances

PAPER

View Article Online
View Journal | View Issue

Cite this: *RSC Adv.*, 2025, **15**, 20084

Unveiling molecular vibrations and anisotropy in semiconductor $PbCrO_4$/LAO films using angle-resolved polarized and temperature-dependent Raman spectroscopy†

Zhiyin Wang,[ab] Jie Liu,[b] Hanjun Zou,[b] Lai Wei,[ab] Tianqi Sun,[bd] Jingwen Zhou*[a] and Xiangnan Gong *[bc]

Received 6th March 2025
Accepted 30th May 2025

DOI: 10.1039/d5ra01615k

rsc.li/rsc-advances

The semiconductor ternary compound lead chromate ($PbCrO_4$) displays promising prospects in pigment and optoelectronic fields. However, previous studies have only focused on its application, neglecting a deep investigation into its molecular vibrational and structural characteristics, such as the influence of interlayer forces. Here, pulse laser deposition was employed for the preparation of highly oriented $PbCrO_4/LaAlO_3$ thin films. Ultra-low-frequency Raman spectroscopy revealed 16 Raman modes of $PbCrO_4$. Meanwhile, angle-resolved polarized Raman spectroscopy, an efficient and nondestructive technique, was used to investigate material anisotropy and orientation. The first-order temperature coefficient values (χ) of $PbCrO_4$ obtained by temperature-dependent Raman spectroscopy were vastly different (from −0.0924 to 0.0053 cm^{-1} K^{-1}). The small χ value is attributed to the weak interlayer van der Waals forces and electron-phonon interactions, indicating a low level of thermal sensitivity. These findings make $PbCrO_4$ an ideal material for crafting high-temperature-resistant pigments and orientation-dependent photocatalysts.

1. Introduction

The recent rapid development of industries has drawn substantial attention toward energy crises and environmental pollution, indicating the need to develop an environmentally friendly and safe energy technology.[1] Efficient utilization of solar energy has become a major research direction because of its multiple advantages, such as abundant reserves and environment friendliness.[2,3] A suitable photocatalyst widely employed in diverse fields beyond solar energy utilization, such as disinfection and pollutant degradation, is necessary to accomplish this goal.[4–8] Recently, chromate has emerged as a photocatalyst and a promising material for solar cells and water splitting, along with potential applications in photoelectric capacitors, owing to its wide absorption range, narrow optical band gap, and high photocatalytic activity.[9–11] Among the chromate family, lead chromate ($PbCrO_4$) has drawn attention because of its excellent stability, hydrophobicity, and pigmentability.[12–14]

Generally, $PbCrO_4$ can be used as a yellow pigment or photovoltaic anode.[12,14,15] Although it is considered a yellow pigment in terms of both brightness value and color saturation value, the addition of phosphor can improve the properties of $PbCrO_4$ significantly.[16] As a type of photoanode, $PbCrO_4$ synthesized *via* the Pechini method not only exhibits remarkable photoactivity, but also experiences a substantial boost in surface charge-transfer efficiency when strategically integrated with partially oxidized graphenes.[17–19] Nevertheless, previous studies have only focused on its application, without deeply exploring its molecular structure, particularly its molecular vibrational characteristics. Raman spectroscopy serves as a rapid, non-destructive, and high-resolution method for analyzing the lattice structure as well as the optical and phonon characteristics of materials.[20–22] Specifically, angle-resolved polarized Raman spectroscopy (ARPRS) and temperature-dependent Raman spectroscopy have been utilized to conduct a thorough analysis of the molecular vibrational properties of $PbCrO_4$.[23] ARPRS, which acquires Raman spectra by changing the angle relationship between polarized incident light and scattered light, enables the investigation of material anisotropy and orientation and can be utilized in diverse areas, such as the study of spatial separation of photogenerated charges in crystals,[24] piezoelectric materials,[25] anisotropic sensors,[26] and

[a]*Hongshen Honors School, Chongqing University, Chongqing 401331, P. R. China*
[b]*Analytical and Testing Center, Chongqing University, Chongqing 401331, P. R. China. E-mail: xiangnan.gong@cqu.edu.cn; enkii@qq.com*
[c]*College of Materials Science and Engineering, Chongqing University, Chongqing 400045, P. R. China*
[d]*Undergraduate School, Chongqing University, Chongqing 401331, P.R. China*

† Electronic supplementary information (ESI) available. See DOI: https://doi.org/10.1039/d5ra01615k

various optical devices.[27] It is also worth noting that temperature not only has a significant impact on the photoelectric activity but also enables an in-depth study of the phonon anharmonicity of materials.[28,29]

In this work, highly oriented $PbCrO_4$ thin films were successfully fabricated by a home-built pulse laser deposition chamber, with quality and uniformity assessed through many advanced characterizations. Then, a systematic Raman spectroscopic study was carried out on the as-fabricated $PbCrO_4$ thin film from the perspectives of both optics and thermodynamics. A total of 16 Raman modes were revealed through ultra-low frequency and multi-wavelength Raman spectroscopy. Additionally, partial Raman vibration modes were identified by the ARPRS technology. In addition, the temperature-dependent Raman spectroscopy revealed a decrease in the χ value of $PbCrO_4$ thin films, stemming from weakened interlayer van der Waals interactions and electron-phonon coupling. These findings will make $PbCrO_4$ an optimal material for crafting the next-generation designs of high-temperature-resistant pigments and orientation-dependent photocatalysts.

2. Experimental section

2.1. Target and substrates

Pb powder and Cr powder (4N, Aladdin) were weighed by stoichiometry and sintered at 823 K for 24 hours at a heating rate of 5 K per minute, followed by natural cooling. Then, the product was ground and re-sintered by the same process to further improve the crystal quality and density. After grounding the sample, the powder was cold-pressed as a target with a diameter of 1 inch and a thickness of 3 mm. The target was re-sintered at 823 K for another 6 hours to further improve the density and uniformity.[30]

2.2. Thin film growth

Thin films were grown using a home-built pulse laser deposition (PLD, CHI-VAC Research & Development Co., Ltd) system equipped with a KrF excimer laser (Coherent, Lambda Physik COMPexPro201F, $\lambda = 248$ nm, repetition rate = 5 Hz). The base pressure of the chamber was kept around 2×10^{-4} Pa. Laser fluence and substrate temperature were optimized between 0.5 and 10 J cm^{-2} and RT ~823 K, respectively. During the film growth process, the distance between the substrate and the target was maintained at approximately 55 mm, and they were kept rotating in opposite directions at a speed of 10 rpm to reduce target erosion and ensure the uniform growth of the films. Prior to thin-film deposition, a pre-sputtering process involving 12 000 laser pulses was executed to eliminate impurities. Subsequently, the high-quality thin films were successfully deposited onto (111) $LaAlO_3$ substrates (HF-Kejing, LAO) with dimensions of 5×5 mm^2.[30]

2.3. Characterizations

High-resolution X-ray diffraction (XRD, Empyrean, PANalytical) with Cu Kα ($\lambda = 1.54056$ Å) radiation was performed to evaluate the lattice parameters and crystalline orientation. The macro-morphology was carried out using a field-emission scanning electron microscope (SEM, SU8600, HITACHI). The micro-surface morphology and roughness of the $PbCrO_4$ thin film were characterized using an atomic force microscope (AFM, Cypher, Oxford Instruments) in the tapping mode within a 5×5 μm^2 area. The crystal structure and chemical composition of the film were analyzed using a high-resolution transmission electron microscope (HRTEM, Talos F200S, ThermoFisher Scientific) coupled with an energy-dispersive spectrometer (EDS).

High-resolution Raman spectra were recorded using a confocal Raman spectrometer (LabRAM HR Evolution, HORIBA) excited with 473 nm, 532 nm and 632.8 nm lasers, respectively, and coupled with an 1800 groove mm^{-1} holographic grating based on the backscattering geometry. Ultralow-frequency (ULF-532, HORIBA) optical components were used to obtain the Stokes and anti-Stokes spectra with a 100× objective lens (N.A. = 0.90). Temperature-dependent Raman spectroscopy was performed from 77 K to 300 K with a 50× long work distance objective lens (N.A. = 0.50) using a 532 nm laser. ARPRS was also based on the backscattering geometry, and the sample was fixed on the stage under the objective. The polarization direction of the incident laser was adjusted using a half-wave polarizer positioned in the beam path. The analyzer located before the spectrometer entrance was oriented along the *y*-axis for the horizontal configuration and along the *x*-axis for the vertical configuration. In all the cases, a silicon crystal was used as a standard for the calibration of the Raman shifts. A low enough laser power (≤0.2 mW) at the surface of the sample and 300 s acquisition time were used to avoid sample damage and enhance the signal-to-noise ratio.

3. Result and discussion

$PbCrO_4$, belonging to the C_{2h} point group, possesses a $P2_1/n$ space group with lattice parameters of $a = 7.12$ Å, $b = 7.43$ Å, $c = 6.79$ Å, and $\alpha = \gamma = 90°$, $\beta = 102.42°$.[31,32] As shown in Fig. S1,† through the cross-sectional SEM, the thickness of the $PbCrO_4$ film is around 330 nm. XRD was employed to identify the crystal structure of the as-grown samples; two main XRD peaks correspond to the $(\bar{1}11)$ and $(30\bar{1})$ planes, confirming that the as-synthesized $PbCrO_4$ sample was a pure phase, while the (111) plane corresponds to $LaAlO_3$ (Fig. 1a). No distinct Bragg peaks were detected when 2θ exceeds 60°. Fig. 1b illustrates the rocking curve, and the full width at half maximum (FWHM), precisely measured at 0.192° through a Gaussian fitting procedure, is a direct reflection of the sample's quality. The narrow FWHM value confirms the excellent quality of the sample under investigation.[33] Furthermore, the reciprocal space map (RSM) is shown in Fig. 1c. The q_x value signifies the scattering vector within the plane, whereas q_z denotes the scattering vector vertical to the plane. It reveals that the single peak of the $LaAlO_3$ substrate aligns with the two peaks of $PbCrO_4$ at the lower left, also ensuring the good quality and epitaxial coherence of the $PbCrO_4$ film.[34] The AFM image of the sample (Fig. 1d and S2†) intuitively shows that the grain orientation of the $PbCrO_4$ thin film is consistent along the arrow direction. Additionally, the

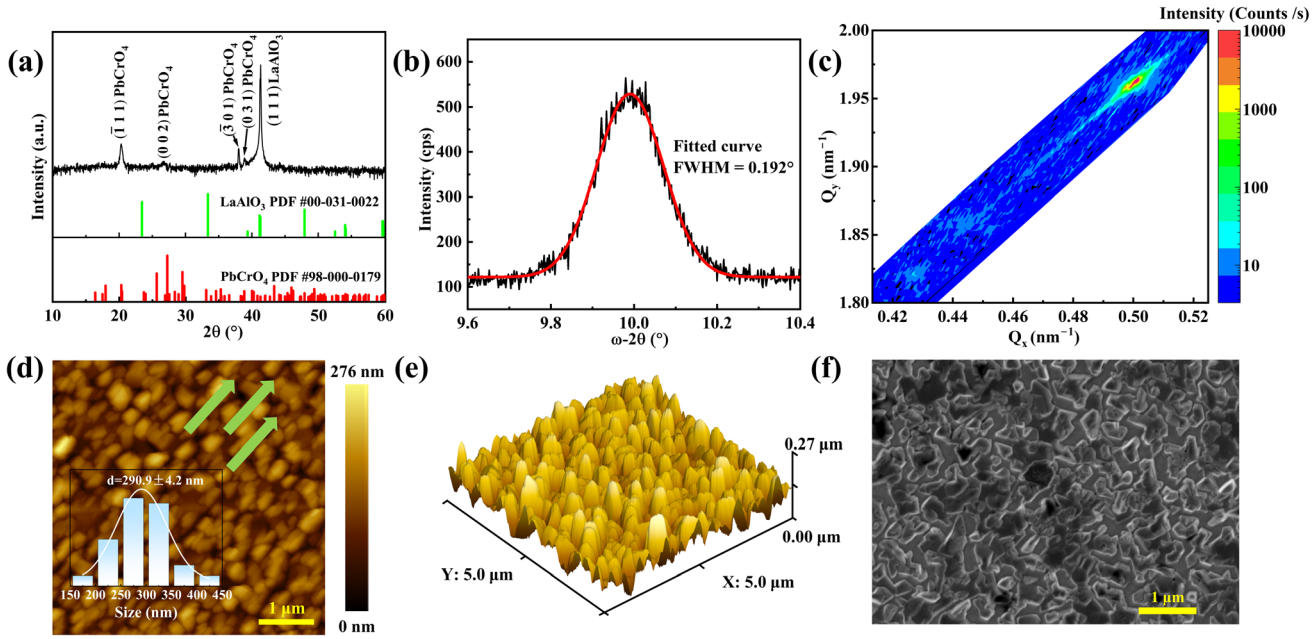

Fig. 1 (a) Experimental powder XRD pattern. Here, the red and green lines denote the standard peaks of $PbCrO_4$ and LAO, respectively. (b) Rocking curve of (1̄11), and (c) RSM image of the $PbCrO_4$/LAO thin film. (d) Two-dimensional (2D) and (e) three-dimensional (3D) AFM images of the sample. Inset: grain size profile. (f) SEM image of the $PbCrO_4$/LAO thin film.

illustration demonstrates that the particle size of $PbCrO_4$ is concentrated at 291 nm. Fig. 1e shows the 3D representation of the AFM image, showing that the grains are consistently columnar and slightly rough. Fig. 1f shows the SEM image of the sample, and the surface of the film is composed of dense irregular $PbCrO_4$ grains, which is a manifestation of the sample belonging to the monoclinic monazite-type structure.

After determining the crystal phases and quality of the sample surface, it is still significant to further explore its internal structure and elemental distribution. Fig. 2a shows the distribution of various elements in the substrate and thin films by EDS, with the high-angle annular dark-field (HAADF) imaging mode. The Pb and Cr elements are concentrated in the $PbCrO_4$ thin film, while La and Al are concentrated in the $LaAlO_3$ substrate. As a common element, O exists in all parts of the sample. At the interface between the thin film and the substrate, all elements exhibit varying degrees of diffusion. Since it is difficult for chemical reactions to occur between $LaAlO_3$ and $PbCrO_4$, this phenomenon should be the irregular diffusion caused by molecular thermal motion.

The EDS results of Fig. 2a indicate a Pb/Cr weight ratio of 19.8%/4.9% (as shown in Table S1†), closely approaching 1/1 when normalized by atomic mass, indicating the high quality of the as-synthesized thin film. Fig. 2b shows the cross-sectional image of the sample. Fig. 2c and d are the HRTEM images and fast Fourier transform (FFT) transformation results of the $PbCrO_4$ thin film, indicating that the crystalline quality of $PbCrO_4$ thin films is superior near the surface compared to that

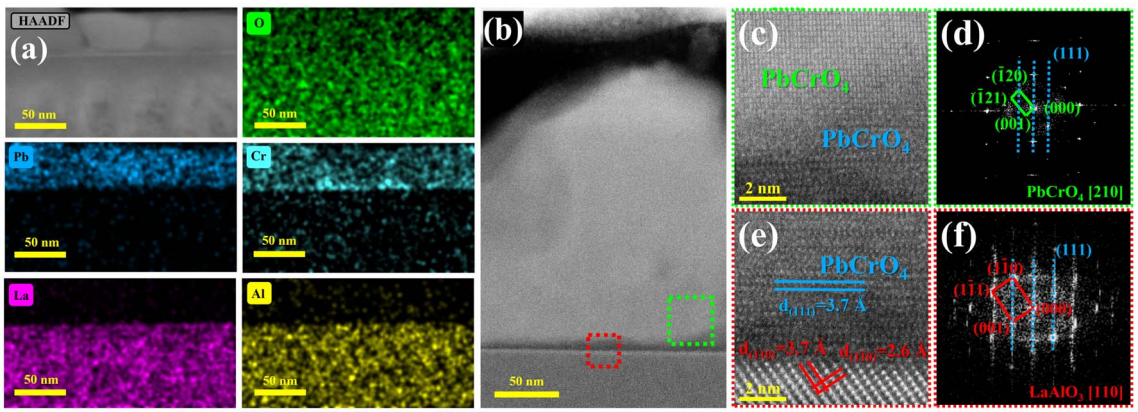

Fig. 2 (a) EDS mapping of each element of the $PbCrO_4$/LAO thin film. (b) Cross-sectional image of the sample. (c and e) HRTEM images and (d and f) FFT transformation images of the green and red rectangles in (b), respectively.

at the interface, as observed in the diffraction pattern obtained from the [210] direction. Fig. 2e and f presents the HRTEM image and FFT transformation results, respectively, of the interface between the substrate $LaAlO_3$ and the initially deposited $PbCrO_4$ thin film. The resolved lattice spacing from the (111) direction of $PbCrO_4$ is 3.7 Å, while for $LaAlO_3$, the resolved lattice spacings are 3.7 Å from the (110) direction and 2.6 Å from the $(1\bar{1}0)$ direction. The diffraction obtained from the [110] direction reveals the presence of $LaAlO_3$ crystals with good crystalline quality, belonging to the trigonal crystal system. The interface $PbCrO_4$ film with a direction of (111) appears in both results, while the surface $PbCrO_4$ film with good crystalline quality is the focus of this study.

Fig. 3a illustrates the experimental setup for the horizontal-polarized and vertical-polarized Raman scattering of the $PbCrO_4$ samples. The crystal coordinates align with the laboratory coordinates without the need for rotating the sample. By rotating the fast axis of the half-wave plate by an angle equal to half of θ, the polarization of the incident laser is rotated by an angle of θ from the y-axis. θ represents the angle between the incident laser polarization and the original polarization of the Raman signal selected by the analyzer's vertical or horizontal polarization signal before entering the spectrometer. To further explore the various structural properties of $PbCrO_4$, Raman spectroscopy analysis was employed. In the inset of Fig. 3a, the gray arrows depict the laboratory coordinate system (x, y, z), whereas the green arrows represent the crystal coordinate system (x', y', z'). The blue two-way arrows indicate the polarization of the incident laser as it reaches the sample. The original polarization of the Raman signal, which corresponds to either a horizontal or a vertical polarized signal selected by the analyzer prior to entering the spectrometer, is denoted by the red two-way arrows.[35] Fig. 3b shows the ultra-low frequency of $PbCrO_4$ thin films. This image includes $\nu\tilde{\nu}_1 \pm \nu\tilde{\nu}_{osc}$, where $\nu\tilde{\nu}_1 = 0$ and $\nu\tilde{\nu}_{osc} = 32, 65, 86, 116, 146, 342\ cm^{-1}$, *etc.* Based on the fundamental principles of Raman scattering, Stokes and anti-Stokes scattering spectra are symmetrically distributed on both sides of the Rayleigh scattering. There is no interference from sample fluorescence peaks in the anti-Stokes section, making it easier to identify Raman peaks. The inset is an enlargement of Fig. 3b from $-500\ cm^{-1}$ to $500\ cm^{-1}$.[36,37] A total of 16 Raman modes were revealed through ULF and multi-wavelength Raman spectroscopy. Fig. 3c shows the Raman spectra of the $PbCrO_4$ thin film under laser irradiation at three wavelengths: 473 nm, 532 nm, and 632.8 nm. It is understood that when the excitation wavelength approaches a specific electronic transition, the nature of Raman scattering undergoes a transformation from the conventional "normal" state to a "resonant" mode, which significantly enhances the intensity of the Raman signal. Notably, the peak at $1669\ cm^{-1}$ conforms to the rule that, as the laser wavelength decreases, the laser energy increases, and consequently, the intensity of the Raman peaks should also increase.

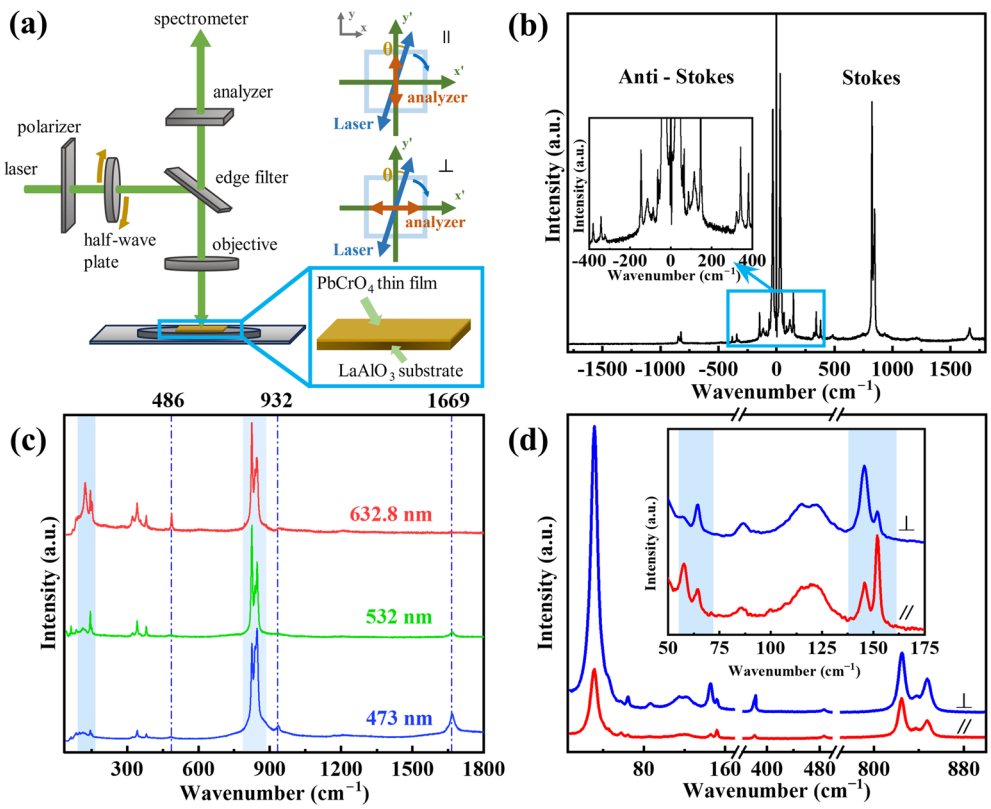

Fig. 3 (a) Schematic diagram of the ARPRS of the $PbCrO_4$ thin film. (b) Stokes and anti-Stokes curves of $PbCrO_4$. Inset: magnified view at ultra-low frequency. (c) Multi-wavelength Raman spectra of the $PbCrO_4$ thin film. (d) Typical Raman spectra under horizontal and vertical polarization. Inset: magnified view from 50 to 175 cm^{-1}.

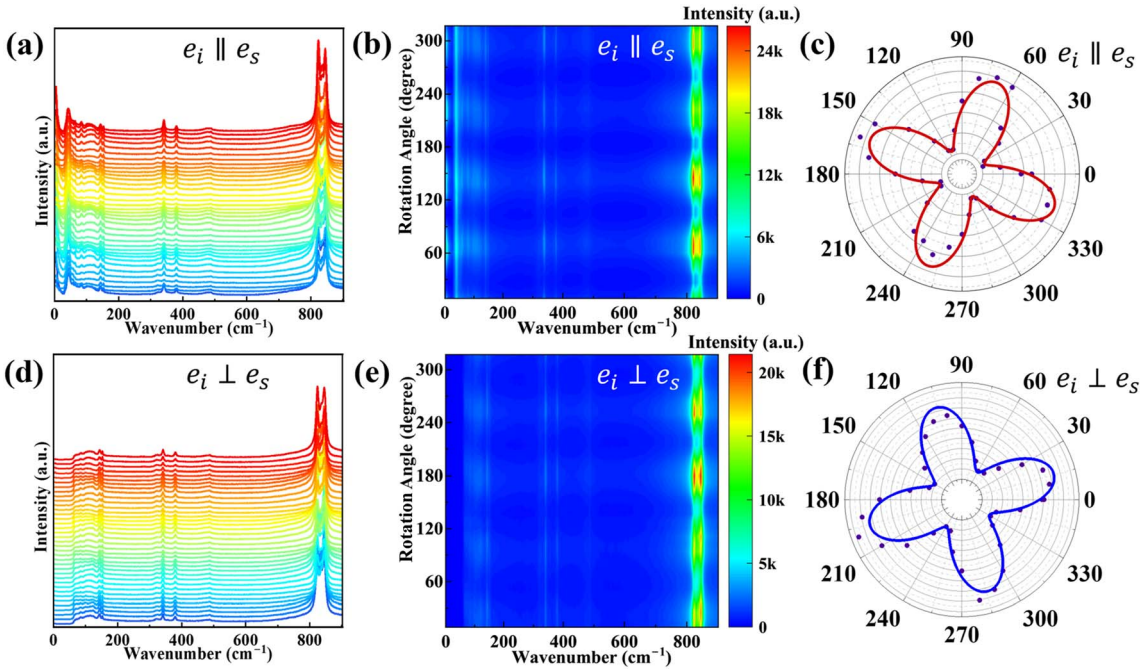

Fig. 4 ARPRS spectra of $PbCrO_4$/LAO thin films under (a) horizontal and (d) vertical scattering geometries. (b and e) Contour color maps of ARPRS results. Raman polarization fitting diagram of the 823 cm^{-1} mode under (c) horizontal and (f) vertical configurations.

However, the intensity changes of the peaks at 486 cm^{-1} and 932 cm^{-1} are contradictory. Meanwhile, within the two marked blue rectangles, the relative intensities of different peaks also vary with the change in laser wavelength. In the resonance process, a particular type of vibrational mode can experience an enhancement in intensity, whereas the intensities of other vibrational modes remain unaffected. In order to reduce the impact of resonance on subsequent experiments, a 532 nm laser with a weak resonance phenomenon was used for the experiment.[38] Fig. 3d shows the Raman spectra obtained under laser

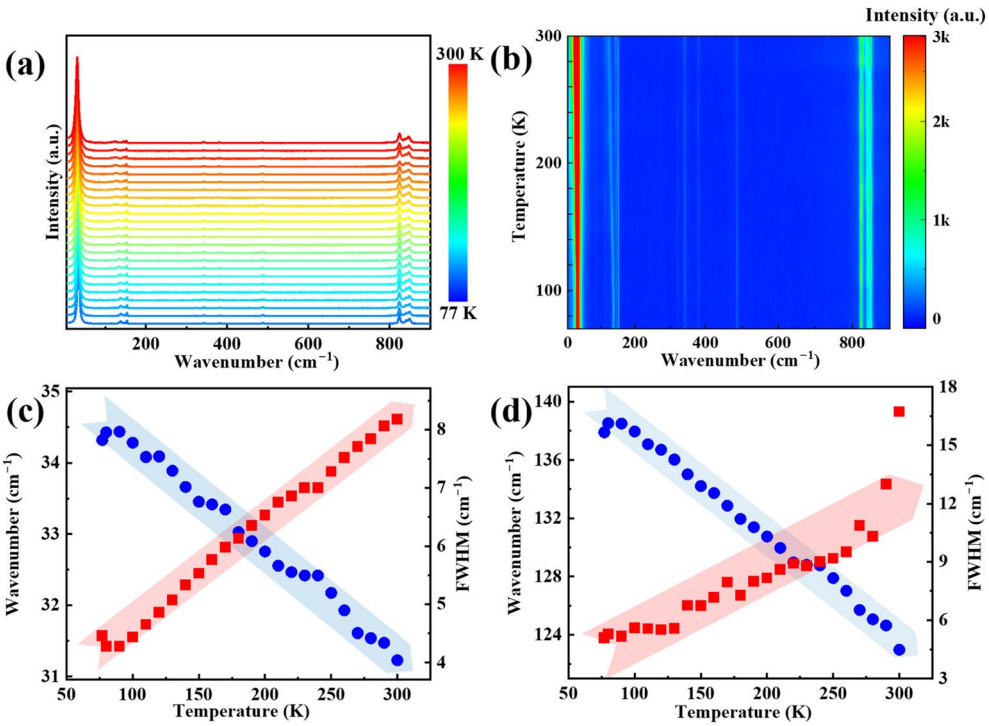

Fig. 5 (a) Temperature-dependent Raman spectroscopy of the $PbCrO_4$/LAO thin film. (b) Contour color map. Peak positions (blue) and FWHM (red) vary with temperature for (c) 34 cm^{-1} and (d) 138 cm^{-1}, respectively.

irradiation with different polarization modes. The differences in Raman peak intensity in Fig. 3d, which are marked by light blue rectangle, indicates the polarization characteristics of the Raman peak, so an ARPRS experiment is needed for the $PbCrO_4$ thin film.

ARPRS is widely used in the study of anisotropy of two-dimensional materials. Laser is incident along the *z*-axis. For the horizontal polarization mode, the reflected polarized light is collected by the polarizer along the *y*-axis, while for the vertical mode, it is collected along the *x*-axis. The experimental setup is shown in Fig. 3a.[35] As $PbCrO_4$ has several types of Raman modes, the intensity of their Raman peaks may vary with the incident angle of the laser, while the Raman intensity is expressed as follows:

$$I \propto \left| \vec{e_i} \cdot \vec{R} \cdot \vec{e_s}^T \right|^2, \quad (1)$$

where R is the Raman tensor, and $\vec{e_i}$ and $\vec{e_S}$ are the unit polarization vectors of the incident laser and scattered Raman signal. The Raman tensor of the $P2_1/n$ space group is expressed as follows:

$$\vec{R}(A_g) = \begin{pmatrix} a & d & 0 \\ d & b & 0 \\ 0 & 0 & c \end{pmatrix}$$
$$\vec{R}(B_g) = \begin{pmatrix} 0 & 0 & e \\ 0 & 0 & f \\ e & f & 0 \end{pmatrix}, \quad (2)$$

where a, b, c, d, e and f are constants. We will obtain their values in the fitting process. When the incident laser propagated along the $\bar{x}$ direction with a unit polarization vector along the $\bar{y}$-axis, we obtained $\vec{e_i} = (\sin\theta \cos\theta\ 0)$. The polarization vector fixed by the analyzer is $\vec{e}_{SH} = (010)$ for horizontal configuration and $\vec{e}_{SV} = (100)$ for vertical configuration. Then, the intensity of A_g mode can be simplified as follows:

$$I(A_g, \parallel) \propto (b\cos\theta + d\sin\theta)^2 \quad (3)$$

$$I(A_g, \perp) \propto (d\cos\theta + a\sin\theta)^2 \quad (4)$$

The intensity of B_g is zero in both vertical and horizontal modes.[35] After obtaining the expected Raman peak intensity variation of the 16 detectable Raman peaks with the incident angle of the laser, a comparative analysis was performed with the experimentally obtained data. Fig. 4a and d show the original polarized Raman spectra. For the sake of visual intuitiveness, Fig. 4b and e intuitively demonstrate the four-periodicity of Raman peak intensity with the angle changes, which can also be found in Fig. 4c and f. The intensities of these Raman modes are functions of the laser incident angle. The scattered dots are experimental data, and the solid lines are fitting curves. Table S2† shows the fitting result of the experimentally obtained data points with calculated formula (3) for horizontal and (4) for vertical. As can be seen from Table S2,† the Raman peak intensity reaches a maximum every 90° of the incident angles of laser, and also has a minimum at ±45° from the angle, where the maximum occurs. The line connecting any two maximal Raman peaks with an angular interval of 180° indicates the direction of the crystal axis. As can be seen from Fig. 4c and f, the angles corresponding to the maxima in the horizontal mode correspond to the angles of the minima in the vertical mode.[39]

Table 1 Temperature-dependent slopes of each Raman peak position and FWHM

No.	Wavenumber (cm^{-1})	Wavenumber slope (cm^{-1}/K)	FWHM slope (cm^{-1}/K)
1	34.5	−0.0160	0.0154
2	137.9	−0.0684	0.0354
3	147.7	−0.0924	0.0379
4	153.7	−0.0089	0.0021
5	342.8	−0.0044	0.0042
6	381.2	−0.0030	0.0038
7	488.2	−0.0066	0.0080
8	823.6	0.0053	0.0016
9	841.0	−0.0134	0.0022
10	848.7	−0.0091	0.0038

Temperature-dependent Raman spectroscopic analysis of the as-synthesized $PbCrO_4$ thin film was performed to investigate its thermal conductivity and phonon behavior, as shown in Fig. 5a. In Fig. 5b, the presence of left-tilted lines indicates a blue shift in the Raman peak positions with the increase in temperature. Concurrently, the FWHM of the Raman peaks increases with temperature. Fig. 5c and d illustrate the linear relationship between both the peak positions and the FWHM with the temperature changed. Fig. S3† summarizes the temperature-dependent variations in the peak positions and FWHM values of individual Raman modes of the $PbCrO_4$ Raman spectra, and the model used to describe these shifts in the $PbCrO_4$ thin film can be expressed as follows:

$$\omega(T) = \omega_0 + \chi T, \quad (5)$$

where ω_0 represents the phonon frequency at 0 K, while χ corresponds to the first-order temperature coefficient of the Raman mode.[40] The slopes of each Raman peak position and FWHM are listed in Table 1. Notably, the Raman peaks at 137.9 cm^{-1} and 147.7 cm^{-1} exhibit significantly larger χ values than the other ones, which are associated with the distribution of electrons and their interactions with phonons.[41] Details can be found in Fig. S4† and the analysis in Support Information. In contrast, the generally smaller values of χ for other modes, compared to other 2D materials, could be attributed to the weaker van der Waals forces between layers in $PbCrO_4$.[28,42]

4. Conclusion

In summary, we have successfully synthesized $PbCrO_4$ thin films on a $LaAlO_3$ substrate by a PLD method. We reported the ULF Raman spectrum of $PbCrO_4$ and clearly identified 16 Raman modes. By ARPRS, precise determination of the location of the crystal axes within the sample became possible, offering

a new approach for non-destructive and rapid determination of the orientation of $PbCrO_4$ thin films. Notably, the weaker van der Waals forces between layers in $PbCrO_4$, coupled with the distribution of charge carriers within the crystal and their interactions with phonons, led to a decreased χ value for $PbCrO_4$. This indicates a lower thermal sensitivity than that of other materials. These findings enrich the understanding of the physical properties of $PbCrO_4$ and offer guidance for the further development of $PbCrO_4$-based materials.

Data availability

All data related to this publication are available either in the main manuscript or its ESI.†

Conflicts of interest

There are no conflicts to declare.

Acknowledgements

This work was financially supported by the Undergraduate Innovation Training Project of Chongqing (S202410611358) and the Large Instrument and Equipment Function Development Project of Chongqing University (gnkf2023010).

References

1 N. Bento, A. Grubler, B. Boza-Kiss, S. De Stercke, V. Krey, D. L. McCollum, C. Zimm and T. Alves, Leverage demand-side policies for energy security, *Science*, 2024, **383**, 946–949.
2 V. K. Jebasingh and G. M. J. Herbert, A review of solar parabolic trough collector, *Renewable Sustainable Energy Rev.*, 2016, **54**, 1085–1091.
3 E. Kabir, P. Kumar, S. Kumar, A. A. Adelodun and K.-H. Kim, Solar energy: Potential and future prospects, *Renewable Sustainable Energy Rev.*, 2018, **82**, 894–900.
4 Q. Wang, T. Hisatomi, Q. Jia, H. Tokudome, M. Zhong, C. Wang, Z. Pan, T. Takata, M. Nakabayashi, N. Shibata, Y. Li, I. D. Sharp, A. Kudo, T. Yamada and K. Domen, Scalable water splitting on particulate photocatalyst sheets with a solar-to-hydrogen energy conversion efficiency exceeding 1%, *Nat. Mater.*, 2016, **15**, 611–615.
5 Q. Xu, L. Zhang, B. Cheng, J. Fan and J. Yu, S-Scheme Heterojunction Photocatalyst, *Chem. Soc. Rev.*, 2020, **6**, 1543–1559.
6 Z. Zhao, Y. Sun and F. Dong, Graphitic carbon nitride based nanocomposites: a review, *Nanoscale*, 2015, **7**, 15–37.
7 H. Wang, L. Zhang, Z. Chen, J. Hu, S. Li, Z. Wang, J. Liu and X. Wang, Semiconductor heterojunction photocatalysts: design, construction, and photocatalytic performances, *Chem. Soc. Rev.*, 2014, **43**, 5234–5244.
8 K. M. Lee, C. W. Lai, K. S. Ngai and J. C. Juan, Recent developments of zinc oxide based photocatalyst in water treatment technology: A review, *Water Res.*, 2016, **88**, 428–448.
9 D. Xu, B. Cheng, W. Wang, C. Jiang and J. Yu, Ag_2CrO_4/g-C_3N_4/graphene oxide ternary nanocomposite Z-scheme photocatalyst with enhanced CO_2 reduction activity, *Appl. Catal., B*, 2018, **231**, 368–380.
10 C. Zhang, X. Tao, W. Jiang, J. Guo, P. Zhang, C. Li and R. Li, Microwave-Assisted Synthesis of Bismuth Chromate Crystals for Photogenerated Charge Separation, *Acta Phys.-Chim. Sin.*, 2023, **40**, 36–46.
11 D. Xu, B. Cheng, S. Cao and J. Yu, Enhanced photocatalytic activity and stability of Z-scheme Ag_2CrO_4-GO composite photocatalysts for organic pollutant degradation, *Appl. Catal., B*, 2015, **164**, 380–388.
12 G.-Q. Zhang, G. Liu, Y. Xu, J. Yang, Y. Li, X. Sun, W. Chen and C.-L. Su, $PbCrO_4$ yellow-pigment nanorods: An efficient and stable visible-light-active photocatalyst for O_2 evolution and photodegradation, *Sci. China Mater.*, 2018, **61**, 1033–1039.
13 L. Cao, X. Fei and H. Zhao, Environmental substitution for $PbCrO_4$ pigment with inorganic–organic hybrid pigment, *Dyes Pigm.*, 2017, **142**, 100–107.
14 A. Zamani, S. Eavani and E. Rafiee, An Environmentally Friendly Yellow Composite Pigment: Leaching Stability and Corrosion Inhibition Properties, *ChemistrySelect*, 2021, **6**, 3833–3840.
15 J. Li, X. Sun, Y. Tian and Y. Zhao, Studies of the Surface Reaction Mechanisms of Pb-3 wt%Sn-0.5 wt%Ag Anode in CrO_3 Solutions, *J. Electrochem. Soc.*, 2013, **160**, E60–E66.
16 Q. Wang, Y. Wang, W. Liu, X. Qiao and T. Seto, Enhancing the color of inorganic yellow pigments using yellow fluorescent materials: The case of $BiVO_4$, $PbCrO_4$/(Y,Gd)AG:Ce^{3+}, Sr_2SiO_4:Eu^{2+}, *Ceram. Int.*, 2024, **50**, 11833–11843.
17 J. Kang, Y. R. Gwon and S. K. Cho, Photoelectrochemical water oxidation on $PbCrO_4$ thin film photoanode fabricated *via* Pechini method: Various solution-processes for $PbCrO_4$ film synthesis, *J. Electroanal. Chem.*, 2020, **878**, 114601–114611.
18 Y. R. Gwon, J. Kang, S. Choe and S. K. Cho, The Photoelectrochemical Response of $PbCrO_4$ Thin Film Fabricated Using Pechini Method: The Effect of Nitrate Decomposition in Precursor Solution, *J. Electrochem. Soc.*, 2023, **170**, 106504–106512.
19 W. Jiang, L. Zhang, C. Ni, M. Shi, Y. Zhao, Y. Deng, H. Chi, R. Chen, X. Wang, R. Li and C. Li, Graphene Mediates Charge Transfer between Lead Chromate and a Cobalt Cubane Cocatalyst for Photocatalytic Water Oxidation, *Angew. Chem., Int. Ed.*, 2023, **62**, e202302575.
20 R. R. Jones, D. C. Hooper, L. Zhang, D. Wolverson and V. K. Valev, Raman Techniques: Fundamentals and Frontiers, *Nanoscale Res. Lett.*, 2019, **14**, 231.
21 X. Zhang, Q. H. Tan, J. B. Wu, W. Shi and P. H. Tan, Review on the Raman spectroscopy of different types of layered materials, *Nanoscale*, 2016, **8**, 6435–6450.
22 S.-Y. Ding, J. Yi, J.-F. Li, B. Ren, D.-Y. Wu, R. Panneerselvam and Z.-Q. Tian, Nanostructure-based plasmon-enhanced Raman spectroscopy for surface analysis of materials, *Nat. Rev. Mater.*, 2016, **127**, 13466–13477.
23 X. Gong, T. Yan, J. Li, J. Liu, H. Zou, B. Zhang, H. Wu, Z. Zhou and X. Zhou, Revealing the anisotropic phonon behaviours

of layered SnS by angle/temperature-dependent Raman spectroscopy, *RSC Adv.*, 2022, **12**, 32262–32269.

24 J. Wu, N. Mao, L. Xie, H. Xu and J. Zhang, Identifying the crystalline orientation of black phosphorus using angle-resolved polarized Raman spectroscopy, *Angew. Chem., Int. Ed.*, 2015, **54**, 2366–2369.

25 L. Li, P. Wen, Y. Yang, N. Huo and J. Li, Improved anisotropy and piezoelectricity by applying in-plane deformation in monolayer WS_2, *J. Mater. Chem. C*, 2021, **9**, 1396–1400.

26 W.-L. Zhu, W.-L. Zhen, R. Niu, K.-K. Jiao, Z.-L. Yue, H.-J. Hu, F. Xue and C.-J. Zhang, Linear dichroism transition and polarization-sensitive photodetector of quasi-one-dimensional palladium bromide, *Chin. Phys. B*, 2024, **33**, 068101–068109.

27 J. Su, W. Shen, J. Chen, S. Yang, J. Liu, X. Feng, Y. Zhao, C. Hu, H. Li and T. Zhai, 2D ternary vanadium phosphorous chalcogenide with strong in-plane optical anisotropy, *Inorg. Chem. Front.*, 2021, **8**, 2999–3006.

28 J. Li, T. Yan, X. Gong, H. Zou, B. Zhang, H. Wu, G. Wang and X. Zhou, Investigation of Temperature-Dependent Phonon Anharmonicity and Thermal Transport in SnS Single Crystals, *J. Phys. Chem. Lett.*, 2023, **14**, 7346–7353.

29 X. Zhang, Y. Liu, G. Zhang, Y. Wang, H. Zhang and F. Huang, Thermal decomposition of bismuth oxysulfide from photoelectric Bi_2O_2S to superconducting $Bi_4O_4S_3$, *ACS Appl. Mater. Interfaces*, 2015, **7**, 4442–4448.

30 H. Zhou, D. Zhang, X. Gong, Z. Feng, M. Shi, Y. Liu, C. Zhang, P. Luan, P. Zhang, F. Fan, R. Li and C. Li, A Dual-Ligand Strategy to Regulate the Nucleation and Growth of Lead Chromate Photoanodes for Photoelectrochemical Water Splitting, *Adv. Mater.*, 2022, **34**, e2110610.

31 J. Gonzalez-Platas, A. Munoz, P. Rodriguez-Hernandez and D. Errandonea, High-Pressure Single-Crystal X-ray Diffraction of Lead Chromate: Structural Determination and Reinterpretation of Electronic and Vibrational Properties, *Inorg. Chem.*, 2019, **58**, 5966–5979.

32 S. K. Ghosh, H. Singh and K. Mallick, Low-dimensional lead chromate-based hybrid system for capacitance and polarization performances: a flexible device for pressure-induced voltage generator, *Emergent Mater.*, 2023, **7**, 235–245.

33 J. M. Tartaglia, S. M. Crochiere, C. E. Kalnas, D. L. Farrington, J. A. Kronwasser and P. J. Pearah, A study of etch pit density and x-ray rocking curves for GaAs substrate evaluation, *J. Electron. Mater.*, 1991, **20**, 345–352.

34 A. K. Panda, A. Singh, R. Divakar, N. G. Krishna, V. R. Reddy, R. Thirumurugesan, S. Murugesan, P. Parameswaran and E. Mohandas, Crystallographic texture study of pulsed laser deposited Cr_2O_3 thin films, *Thin Solid Films*, 2018, **660**, 328–334.

35 X.-L. Liu, X. Zhang, M.-L. Lin and P.-H. Tan, Different angle-resolved polarization configurations of Raman spectroscopy: a case on the basal and edge plane of two-dimensional materials, *Chin. Phys. B*, 2017, **26**, 067802–067810.

36 P. Tan, L. An, L. Liu, Z. Guo, R. Czerw, D. L. Carroll, P. M. Ajayan, N. Zhang and H. Guo, Probing the phonon dispersion relations of graphite from the double-resonance process of Stokes and anti-Stokes Raman scatterings in multiwalled carbon nanotubes, *Phys. Rev. B*, 2002, **66**, 245410–245418.

37 R. Loudon, The Raman effect in crystals, *Adv. Phys.*, 2001, **50**, 813–864.

38 Z. Wu, Multi-wavelength Raman spectroscopy study of supported vanadia catalysts: Structure identification and quantification, *Chin. J. Catal.*, 2014, **35**, 1591–1608.

39 X. Zhao, Z. Yang, J. Guo, X. Zhong, W. Dou, Y. Yin, Y. Peng, R. Zeng, W. Zhou, D. Tang and Y. Zhou, Anisotropic Electron–Phonon Interactions and Crystallographic Orientation Identification in Ta_2NiSe_7 Thin Flakes, *J. Phys. Chem. C*, 2022, **126**, 12635–12642.

40 A. C. Dakshinamurthy and C. Sudakar, Sublattice Distortion Enabled Strong Interplay between Phonon Vibrations, Electron-Phonon Coupling, and Self-Trapped Excitonic Emissions in $Cs_2Ag_{1-x}Na_xBiCl_6$ Double Perovskites, *J. Phys. Chem. Lett.*, 2022, **13**, 433–439.

41 U. F. Kaneko, M. D. Teodoro, P. F. Gomes, N. S. Sangeetha and D. C. Johnston, Electron-phonon coupling enhancement and displacive magnetostructural transition in $SrCr_2As_2$ under magneto-Raman spectroscopy, *J. Phys.: Condens. Matter*, 2021, **33**, 105401.

42 P. M. Pataniya, M. Tannarana, C. K. Zankat, S. A. Bhakhar, S. Narayan, G. K. Solanki, K. D. Patel, P. K. Jha and V. M. Pathak, Low-Temperature Raman Investigations and Photoresponse of a Detector Based on High-Quality WSe_2 Crystals, *J. Phys. Chem. C*, 2020, **124**, 2251–2257.